

Development of an *in situ* underwater particle image velocimetry (UWPIV) system

Qian Liao¹*, Harvey A. Bootsma², Jianen Xiao¹, J. Val Klump², Andrew Hume³, Matthew H. Long³, and Peter Berg³

¹Department of Civil Engineering and Mechanics, University of Wisconsin-Milwaukee, Milwaukee, WI 53211, USA

²Great Lakes WATER Institute, University of Wisconsin-Milwaukee, Milwaukee, WI 53204, USA

³Department of Environmental Sciences, University of Virginia, 291 McCormick Road, Charlottesville, VA 22904, USA

Abstract

A low-cost self-contained underwater particle image velocimetry (UWPIV) system has been developed to measure small-scale turbulent flow structures *in situ*. The UWPIV employs a compact continuous-wave laser and an optical scanner to deliver a light sheet that illuminates naturally occurring particles. Particle images are taken by a CCD camera along with an ultra-compact PC. The nontethered and compact design can be fit in two small underwater housings with all components powered by batteries: an ideal design for a variety of *in situ* deployments. The system has been field-tested in the coastal zone of Lake Michigan. Turbulent flow structures of the wave-current bottom boundary layer are measured right above the nearshore lakebed, which is densely covered by quagga mussels (*Dreissena bugensis*). Vertical profiles of mean velocity, Reynolds stresses, dissipation rate of the turbulent kinetic energy, turbulent viscosity, plankton particle concentration, and the turbulent flux of particles are presented and discussed.

Introduction

Digital particle image velocimetry (DPIV) has become a popular measurement technology for fluid flows since it was introduced in the early 1990s (Adrian 1991; Willert and Gharib 1991). Since PIV can resolve the two dimensional (2D) distribution of two (or three) components of velocity instantaneously, it is ideal for characterizing spatial structures of turbulent flow, e.g., the distribution of the turbulent kinetic energy (TKE), Reynolds stresses, TKE production and dissipation, as well as the coherent structure of turbulence. For this reason, PIV is preferable to single-point measurement instruments, such as the Acoustic Doppler Velocimeter (ADV) and Laser Doppler Velocimetry (LDV), and velocity profilers such as the Acoustic Doppler Current Profiler (ADCP). Most PIV applications in water flows have been limited to laboratory studies. It is challenging to deploy a PIV system in a natural aquatic environment, as it requires configuration in submersible housings.

A typical PIV system employs a powerful pulsed laser (usually a dual-head Q-Switched Nd:Yag laser) with a bulky power supply unit and a dedicated computer system for image acquisition. Such a system is generally restricted to lab deployment, and configuration for underwater deployment can be both costly and awkward. During the past few years, a partially submersible PIV system has been built and successfully deployed in coastal oceans (Bertuccioli et al. 1999; Doron et al. 2001; Nimmo Smith et al. 2002, 2005; Luznik et al. 2007). This system employed a flash lamp pumped dye laser to generate laser pulses with 120 mJ of light energy per pulse at a wavelength of 594 nm. Only the CCD camera was fully submerged, while the laser unit and the computer system were kept above the water surface (on a ship). Laser light was delivered through optical fibers to the underwater flow field.

More recently, several self-contained *in situ* PIV systems have been developed, taking advantage of the advancements in compact diode-pumped solid state (DPSS) laser technologies (Steinbuck et al. 2004; Clarke et al. 2007; Katija and Dabiri 2007). Due to its high energy efficiency, a DPSS laser can be powered with batteries thus eliminating the need for a massive power supply unit. However, all battery-operated DPSS lasers are continuous wave (CW) lasers. To get an “unblurred” image of moving particles, all published *in situ* PIV systems with DPSS lasers have used camera shutters to control the exposure time of reflective particles. As a result, the light density delivered per exposure is, at most, an order of magnitude

*Corresponding author: E-mail: liao@uwm.edu

Acknowledgments

We are very grateful for the assistance provided by Geoff Anderson, Randy Metzger, and Craig Barske in the construction of the underwater PIV system. We appreciate the support provided by Capt. G. Stamatelakys, J. Weselowski, and the rest of the crew of the RV *Neeskay*. We are also thankful to two anonymous reviewers for their helpful comments and suggestions.

smaller than that from a typical Q-switched laser. Thus, they are limited to applications where either the flow speed is extremely slow to afford a longer exposure time or the size of seeding particles is larger to scatter more light.

In this paper, we present an alternative solution: a compact and self-contained underwater PIV (UWPIV) system that can greatly simplify deployments in field experiments. Using a CW DPSS laser combined with an optical scanner, the UWPIV can provide much more illumination to particles without the need of higher laser power and can avoid blurred particle images at the same time. As a proof of concept, we demonstrate that the UWPIV can be applied to characterize the hydrodynamics of the bottom boundary layer in coastal Lake Michigan. Moreover, we examined the effects of dreissenid mussels (the zebra, *Dreissena polymorpha*, and the quagga mussels, *Dreissena bugensis*) on benthic particle flux through seston consumption. The UWPIV system presented in this paper provides quantitative data that parameterizes the benthic turbulent mixing induced by ambient currents and mussel filtering activities.

Materials and procedures

Laser light illumination and seeding particles—A successful PIV measurement relies on delivering adequate illumination to seeding particles in fluid flows. Most PIV systems adopt a pulsed laser (e.g., a dual head Q-Switched Nd:Yag laser) to generate a 2D light sheet. The typical duration of laser pulses is on the order of tens of nanoseconds, with a light intensity of tens or hundreds millijoules. The intense light ensures that small seeding particles can be illuminated to a detectable level for CCD sensors, and the short light pulse “freezes” the moving particle such that they do not appear as streaks in the image. The average intensity of a particle’s image is linearly proportional to the optical exposure of the particle, which is defined as the average light energy per unit area on a CCD sensor array. The optical exposure is a function of the energy of the incident light, the particle’s diameter, its Mie scattering parameter, and the optical configuration.

Adrian (1991) estimated that for a typical optical system of PIV (illustrated in Fig. 1), the mean optical exposure averaged over a particle’s image, denoted as I , is proportional to

$$I \sim \frac{W}{L\delta} \frac{d_p^3 D_a^4}{M^2 d_o^2 \lambda^3} \quad (1)$$

for particles in the 1~10 μm range, i.e., particle diameter is comparable to the wavelength of the incident light, and

$$I \sim \frac{W}{L\delta} \frac{D_a^2}{M^2 d_o^2} \quad (2)$$

for particles in the geometrical scattering range, on the order of 10~100 μm . In the above two equations, W is the energy of the incident light, L and δ are the expansion and thickness of the laser light, λ is the wavelength of the incident light, d_o and d_i are the object and image distance from the lens, $M = d_i/d_o$.

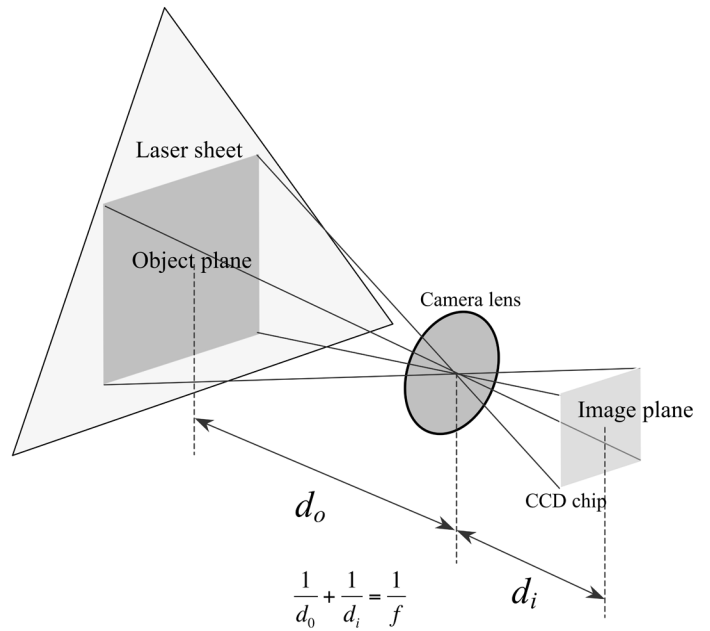


Fig. 1. Optical configuration of a PIV imaging system.

the magnification, and D_a is the lens aperture, which can be estimated by $D_a = f/\#$, where f is the focal length, $\#$ is the f-number of the camera lens, and

$$\frac{1}{f} = \frac{1}{d_o} + \frac{1}{d_i} \quad (3)$$

Although particle seeding is possible while deploying the UWPIV system in situ, it is always more convenient to use natural particles as seeding tracers, such as plankton and suspended sediment. The concentration and size distribution of these particles are highly variable in natural waters. According to Bertuccioli et al. (1999), the concentration of particles in the 10 μm range is always sufficient for PIV measurements even in clean ocean water. Our own experience in Lake Michigan also verifies that there is always sufficient amount of small (10 μm range) particles under clear water conditions, while larger particles (100 μm range) can be present in high concentration under fairly turbid conditions. Therefore, the illumination light for PIV needs to be strong enough that a sufficient number of small particles (of the order of 10 μm) can be imaged to ensure an adequate seeding density for PIV interrogations.

It is difficult to determine the minimum light density required for an in situ PIV system, as many other factors are included such as the composition of the particles, the viewing angle of the camera relative to the light plane, the sensitivity of the CCD sensor (e.g., the “quantum” efficiency), and the turbidity of water. Bertuccioli et al. (1999) estimated that a 50 mJ light sheet is adequate to generate a clear image of a 10 μm particle, although details were not provided for the type of lens, camera and light sheet thickness and width. It should be noted that the required light energy is approximately a cubic

function of the diameter of particles in the 1~10 μm range as indicated by Eq. 1. Our own experience in Lake Michigan suggested that a 10 mJ light sheet is necessary for a good PIV measurement with a field of view (FOV) of 13×13 cm, using a camera lens with $f = 50$ mm and $\# = 1.4$. We have used this experience as a criterion to estimate the required light energy and camera lens for different sizes of FOV, following Eqs. 1-3.

For a typical laboratory PIV system with a Q-Switched laser, the laser beam is expanded by a cylindrical lens to generate a light sheet. This is also applicable for a CW laser. However, we have opted to use a galvanometer (i.e., laser beam is steered by a rotating mirror) to scan the CW laser beam, forming a “sheet” of light. Fig. 2 shows the general timing diagram of signal waves that control the angle of the rotating mirror and the exposure time of the digital camera in such a PIV system, where T_s is the time of one sweep and T_d is the time between the end of one sweep and the beginning of the following sweep. The time T_d depends on the hardware of a CCD chip: it needs to be longer than the time required for image data being transferred from the CCD chip to the storage memory. Therefore, the elapsed time that separates two exposures of every tracer particle in the object plane is $\Delta T = T_s + T_d$. It is equivalent to the time lag between two laser pulses in a traditional PIV system.

For a turbulent flow measurement, ΔT should be small enough to reduce the loss of particle pairs due to out-of-plane motions, i.e., particles traveling in a direction oblique to the light plane. On the other hand, T_s should be kept as large as possible to maximize the effective energy of illumination, i.e., $W = PT_s$, where P is the power of the CW laser. This can be explained by considering the following three light sheet generation schemes each of which generates a light sheet with the same width (L) and thickness (δ): scheme A is a pulsed laser beam expanded by a cylindrical lens delivering a total energy of (W) to the field to be illuminated; scheme B is a CW laser of power P_B with the same cylindrical lens and the exposure time for the camera is set to T_E ; and scheme C is a CW laser of power P_C scanned by a galvanometer with a sweeping time of T_s . Thus, it is required that $P_B = W / T_E$ in scheme B, and $P_C = W / T_s$ in scheme C to produce the same amount of illumination energy in scheme A. The advantage of scheme C over B can be illustrated through the following example. For scheme B, it is of prime importance that T_E be short enough to avoid blurred images of moving particles. Ideally the length of the “streak” line of the particle image should be smaller than its diameter on the image, d_{pi} , in which case $T_E < d_{pi}/u$, where u is the speed of the moving particle. For a typical $d_{pi} = 0.2$ mm (i.e., 2 pixels for a 1024×1024 CCD sensor array imaging a field of $L = 10$ cm), and $u = 10 \text{ cm s}^{-1}$ in an environmental flow, $T_E < 2$ ms is required. Thus the laser power P_B needs to be greater than 5 W to be equivalent to the 10 mJ/pulse energy in scheme A. For scheme C, the exposure time of a particle can be approximated by $\delta T_s / L$, assuming that the speed at which the light beam passes through the particle is much greater than u .

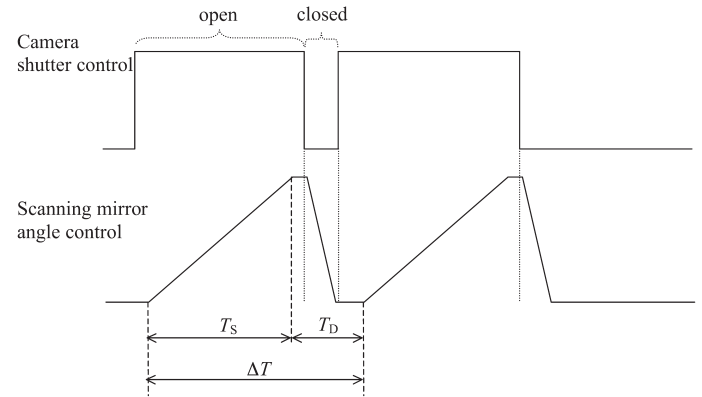


Fig. 2. Timing diagram of voltage signals that synchronize the camera shutter and the galvanometer (rotating mirror).

When the exposure time equals that in scheme B, we have

$$\frac{T_s}{T_E} = \frac{L}{\delta} \quad (4)$$

Thus $T_s < 100$ ms is sufficient (assume $\delta = 2$ mm, $L = 10$ cm, $d_i = 0.2$ mm, and $u = 10 \text{ cm cm s}^{-1}$) to “freeze” the particle on image. Accordingly, the laser power P_C only needs to be greater than 0.1 W to generate the illumination energy that is equivalent to 10 mJ/pulse in Scheme A.

Usually, the maximum value of T_s is limited by the strength of the out-of-plane turbulent motion, since $T_s < \Delta T$. For example, a velocity fluctuation of $u_f = 5 \text{ cm s}^{-1}$ is considered to be a strong turbulent motion in a coastal boundary layer flow. Assume a laser sheet that has a thickness of $\delta = 2$ mm and is parallel to the mean current, $T_s < \Delta T < \delta/u_f = 40$ ms is required to keep the interrogation error small. In general, $\Delta T \sim O(10)$ ms is a good choice for many environmental flow applications. It should be noted that it is often not possible to align the light plane exactly with the mean flow as the mean current direction may shift during an in situ deployment.

Laser sheet generation with a galvanometer has been widely used in planar laser-induced fluorescence (PLIF) techniques, which can be applied to measure the turbulent scalar concentration field (Cowen et al. 2001). It is preferable to cylindrical lens expansion of a single beam since the light energy is more uniformly distributed. For turbulent velocity measurements, it is less desirable than a pulsed laser, as particles on a PIV image are not recorded at the same instance. Nonetheless, in most applications, the sweeping time is usually small (an order of 10 ms) compared with the integral time scale of turbulent “eddies,” which is comparable in size with the FOV for most environmental flow. Therefore, errors associated with the asynchronous illumination are often negligible.

Component and layout of the UWPIV system—For the UWPIV system presented in this paper, we choose a handheld DPSS laser (Hercules 375 from LASERGLOW.COM). It emits a 375 mW CW laser beam at 532 nm. The laser beam is swept by a

compact moving magnet closed loop galvanometer (Cambridge Technology, Model 6210). Particle images are taken by an Imperx IPX-4M15-G CCD camera, with $7.4 \times 7.4 \mu\text{m}$ pixel size, a resolution of up to 2048×2048 pixels and a maximum frame rate of 15 Hz at the full resolution (30 Hz at the resolution of 1024×1024). This camera digitizes acquired images to a format of 12-bit pixel depth and can be streamed directly to a computer through a Gigabit Ethernet (GigE) interface. A SONY UX390N Micro PC is used for image acquisition as well as controlling the PIV system. It is a full-fledged compact computer ($150 \times 95 \times 40$ mm in size) equipped with an Intel Core Solo CPU at 1.33 GHz, 1 GB of DDR2 memory and a 32 GB solid state drive (SSD) hard drive. The available storage space of the computer is 15 GB with the space allocated for the operating system and applications excluded. If image pairs are acquired at 1 Hz (4 MB per second), it allows 1 hour of time series acquisition. This limit can be extended to 6 hours by directly storing images on an external 64GB SSD through the computer's USB port. Voltage signals that control the galvanometer and trigger the digital camera, as shown in Fig. 2, are sent out through two Analog Output ports of an USB-based data acquisition (DAQ) module (DataTranslation DT9812-10V). The DAQ module is connected to the SONY compact PC and programmed with MATLAB (MathWorks, Inc.) data acquisition toolbox.

The CCD camera, ultra-compact PC and the DAQ module are fitted into one underwater camera housing (Aquacam Ex from Aquatix International), making up the imaging unit. The laser, galvanometer and associated optics are fitted into another housing (Equinox Pro8) to make the illumination unit. The two units are mounted on a steel tripod frame (see Fig. 3). An underwater cable that transmits control signals from the two AO ports to the galvanometer penetrates the two housings through waterproof bulkhead connectors (BIRNS Aquamate connectors). In order to block out the ambient light, a narrow band-pass optical filter (with full-width at half-maximum, FWHM = 3 nm) is placed in front of the CCD chip. Although the overall signal strength is reduced by about 70% (the peak transmissivity of the band-pass filter is about 30%), it does not affect the quality of PIV interrogations. With the filter, the system can collect particle images even on a very sunny day just below the lake surface. All components are powered by Li-ion battery packs, and the total weight is less than 5 kg (excluding the underwater housing). The estimated overall power consumption is between 30W to 40W, depending on the image sampling rate.

The distance from the laser sheet to the camera lens can be adjusted to be between 15 and 65 cm. As the CCD imager area is 15×15 mm, we are able to adjust the range of FOV to be between 3×3 cm (with a $f=105$ mm Nikon lens) and 80×80 cm (with a 12 mm Nikon lens). In the study described here, the distance is set to 48 cm. A Nikon lens (50 mm, f1.4) is used making the FOV about 13.6×13.6 cm. Before field deployment, the focus of the image system is adjusted in the laboratory.



Fig. 3. Underwater housings and supporting tripod frame of the UWPIV system.

A large fish tank filled with lake water is placed in front of the imaging housing to account for the refraction effect. Meanwhile the actual FOV can be calibrated by taking a picture of a ruler placed right on the object plane.

Deployments—The UWPIV system was deployed in the nearshore waters of the western Lake Michigan, about 8 km north of the Milwaukee Harbor and 500 meters offshore from the Atwater Park of the City of Milwaukee, Wisconsin. The local water depth is about 10 meters and the rocky bottom is densely covered by quagga mussels. For each deployment, a SCUBA diver carries the device to the bottom of the lake and carefully adjusts the position of the system such that the laser light sheet is perpendicular to the lake bottom and nearly parallel to the mean flow direction to minimize the out-of-plane particle motion. However, this is not always possible as the mean current may change direction in a few minutes. In addition, the water depth at the deployment site was shallow enough to be strongly affected by surface waves. Wave induced near bottom motion may not always align with the mean current direction. As a result, correlation of particle images was lost in some image pairs recorded.

Three data sets were acquired through preliminary deployments on 31 August 19 September and 20 September 2007, and they will be referred to as datasets A31, S19 and S20 hereinafter. The hydrodynamic conditions on the 3 days were very different: on 31 August, a steady current with very little wave motion was observed near the bottom; on 19 September, the near-bed flow was dominated by oscillating surface waves with nearly zero mean current; on 20 September, a strong current was observed, superimposed by strong surface wave induced motions. The concentration and size distribution of particles in the water also varied among dates. On 31 August, the water was warm and well mixed, about 20°C throughout the water column. Through image processing,

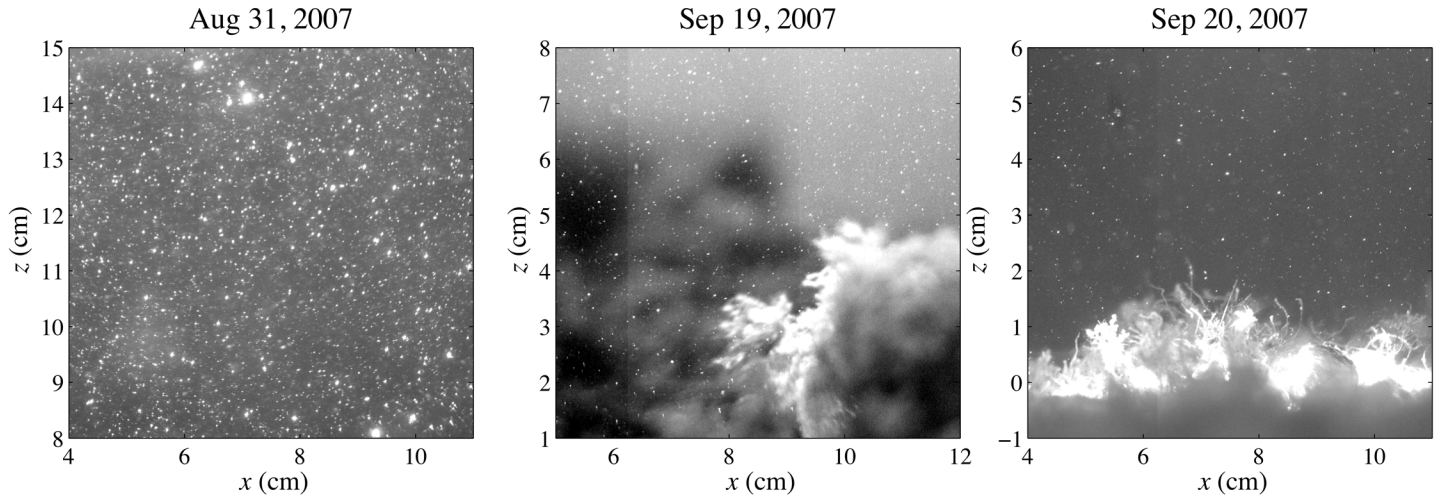


Fig. 4. Sample PIV images acquired in three preliminary deployments in Lake Michigan. Shadows in images of 19 Sep 2007 are bed structures on the background (away from the object plane, unfocused). They are removed before PIV interrogations. The bed structure on the lower-right corner is in between the object plane and the camera lens. It is masked out from images before PIV interrogations. Quagga mussels with *Cladophora* (a filamentous algae) on their shells can be identified in images of 20 Sep 2007. For all image sets, $z = 0$ is defined to be at the lake bed.

the number concentration of particles that can be identified from images was about 250 per milliliter and the average diameter was about 100 μm (procedures of particle identification will be shown later). On 19 and 20 September, the water column was also well mixed at the deployment site, but the temperature was quite low ($\sim 5^\circ\text{C}$) due to a strong upwelling event. Water clarity was very high during these 2 days, thus the particle concentration was much lower (about 90 per milliliter) and the average particle diameter was much smaller (30 μm). Fig. 4 shows example PIV images of the three deployments under the same illumination and exposure configurations: $T_s = 26$ ms and $\Delta T = 30$ ms. For all the three deployments, the sampling rate was set to 1 Hz, i.e., one image pair per second. The FOV in the experiments was actually 13.6 cm \times 13.6 cm and the size of an image was 1024 \times 1024 pixels under a 2 \times 2 binning mode. With CCD binning the signal to noise ratio can be improved and the data rate can be reduced without reducing the FOV, while the effective imager pixel size is doubled to 14.5 μm . Since the lake bottom at the deployment site was rocky and uneven, the diver was not always able to position the system ideally such that the lake bottom is included in the image. In A31 images, the bottom edge of the image was about 7 cm above the lakebed; for S19, the bed was 1 cm below the imaged field; for S20, the bed was visible in the image as shown in Fig. 4(C).

The size of PIV interrogation subwindows is chosen to maximize particle image correlations without loss of spatial measurement resolution. A resulting vector is deemed invalid if the correlation coefficient is less than 50%, and is discarded. The discarded vector is replaced by the local median value calculated based on a 4 \times 4 vector map stencil. For all the three data sets, subwindows were overlapped by 50%. Parameters

including the subwindow size, grid distribution of the velocity vector map, spatial resolution and the overall performance of PIV interrogations are listed in Table 1. We found that the quality of PIV interrogation depends on the seeding density and the severity of out-of-plane flows. Data set S20 has the highest number of invalid vectors, possibly due to the loss of correlation as a result of misalignment between the laser light sheet and the mean current/wave induced motion, which is much stronger on 20 September, compared to that on 31 August and 19 September. Reducing the time lag between two exposures, Δt , might have helped to alleviate this problem. The average TKE dissipation rate (detailed in the Assessment section) and the Kolmogorov length scale of the turbulence are also listed to check whether the measurement resolution is high enough to reveal the smallest turbulence structures. Fig. 5 shows a sample instantaneous velocity field resulting from PIV interrogations on the data set of S19.

The time series of streamwise velocity (along the direction of the mean current) measured at $z = 8$ cm during the S19 and S20 deployments is shown in Fig. 6. These velocities are horizontally averaged values over a row of PIV grid points, i.e., over 11.7 cm. A low pass-filter of the time series is also applied to remove the wave-induced motions and to show the temporal variation of the mean current speed (shown as bold lines in Fig. 6). In order to validate the PIV measurements, an ADV probe was also deployed immediately next to the PIV system on S19. The sample volume of the ADV is about 12 cm above the bed and 1 m apart from the PIV laser plane in the cross-stream direction. Fig. 7 shows the comparison between the time series of the ADV measurement and that of the PIV measurement at $z = 12$ cm. Considering the fact that the two devices are 1 m away from each other, the agreement between the two time series is excellent.

Table 1. PIV interrogation parameters, performance of the PIV analysis, and the overall turbulent flow characteristics of the three datasets acquired on 31 Aug 2007, 19 Sep 2007, and 20 Sep 2007

Data set	A31	S19	S20
Pixel size of PIV interrogation subwindow	32×32	40×40	40×40
Grid of the velocity vector map (rows \times columns)	60×52	45×45	35×45
Spatial resolution (mm)	2.125	2.656	2.656
Duration of measurements (s)	62	785	869
Average number of particles in a 32×32 subwindow	11	4	4
Percentage of valid velocity vectors	98.9%	95.4%	81.5%
Mean current speed at $z = 7$ cm (cm s^{-1})	3.8	0.28	7.3
Mean dissipation rate $\times 10^6$ ($\text{m}^2 \text{s}^{-3}$)	12.24	2.74	46.64
Kolmogorov length $\eta = \left(\frac{\nu}{\epsilon} \right)^{1/4}$ (mm)	0.54	1.05	0.52

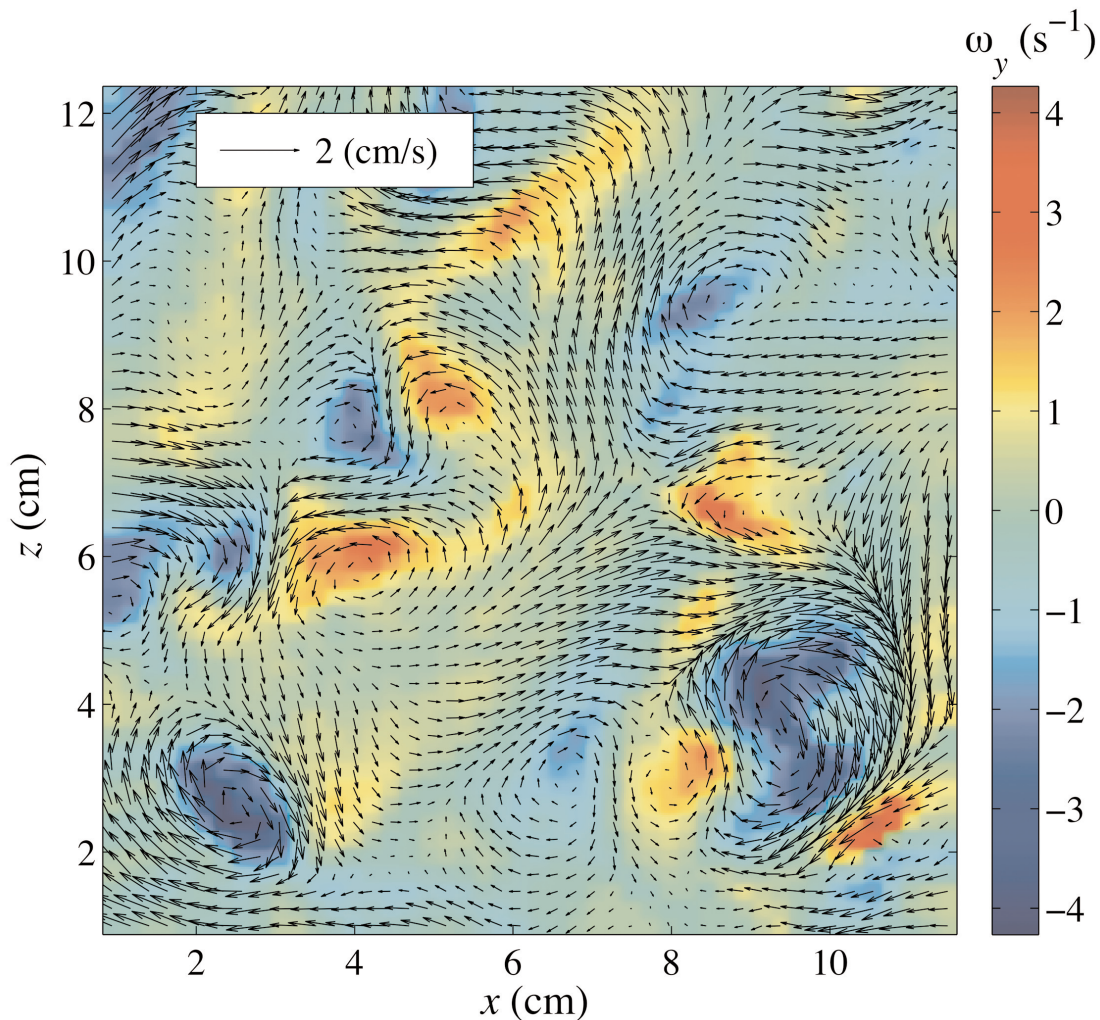


Fig. 5. A sample of instantaneous 2D velocity field revealed by PIV interrogations (from the S19 data set), superimposed on the map of the calculated vorticity $\left(\omega_y = \frac{\partial w}{\partial x} - \frac{\partial u}{\partial z} \right)$ from the measured velocity distribution. The areal averaged values over the velocity map are $\langle u \rangle = 4.1 \text{ cm s}^{-1}$ and $\langle w \rangle = -1.1 \text{ cm s}^{-1}$. They are subtracted from the instantaneous velocity field to show vortical structures of the turbulent flow.

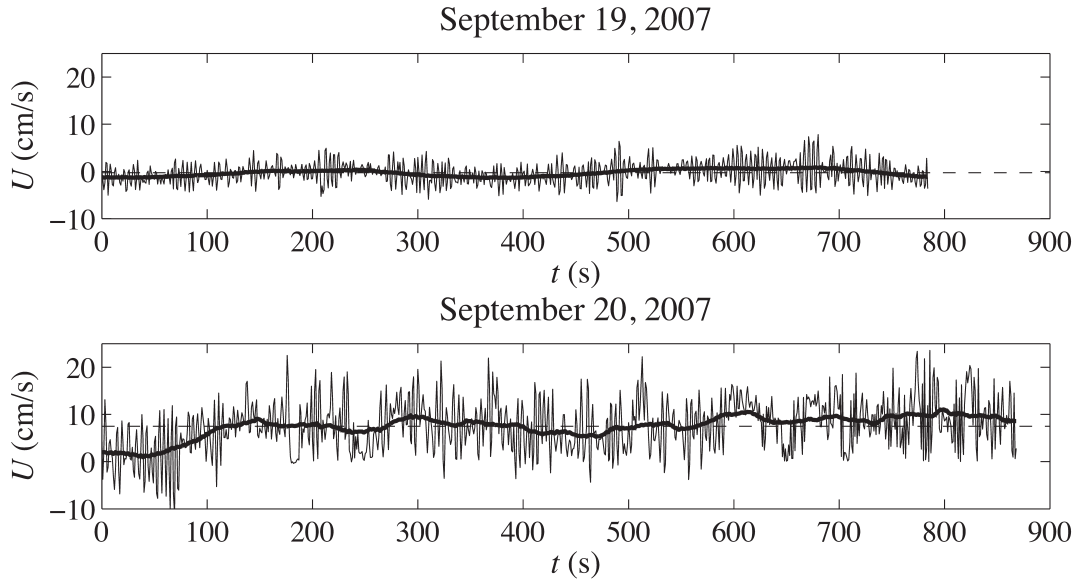


Fig. 6. Time series of the streamwise velocity at $z = 12$ cm measured by PIV on 19 and 20 Sep 2007. The bold line represents the low-pass filtered (> 50 s) velocity signal.

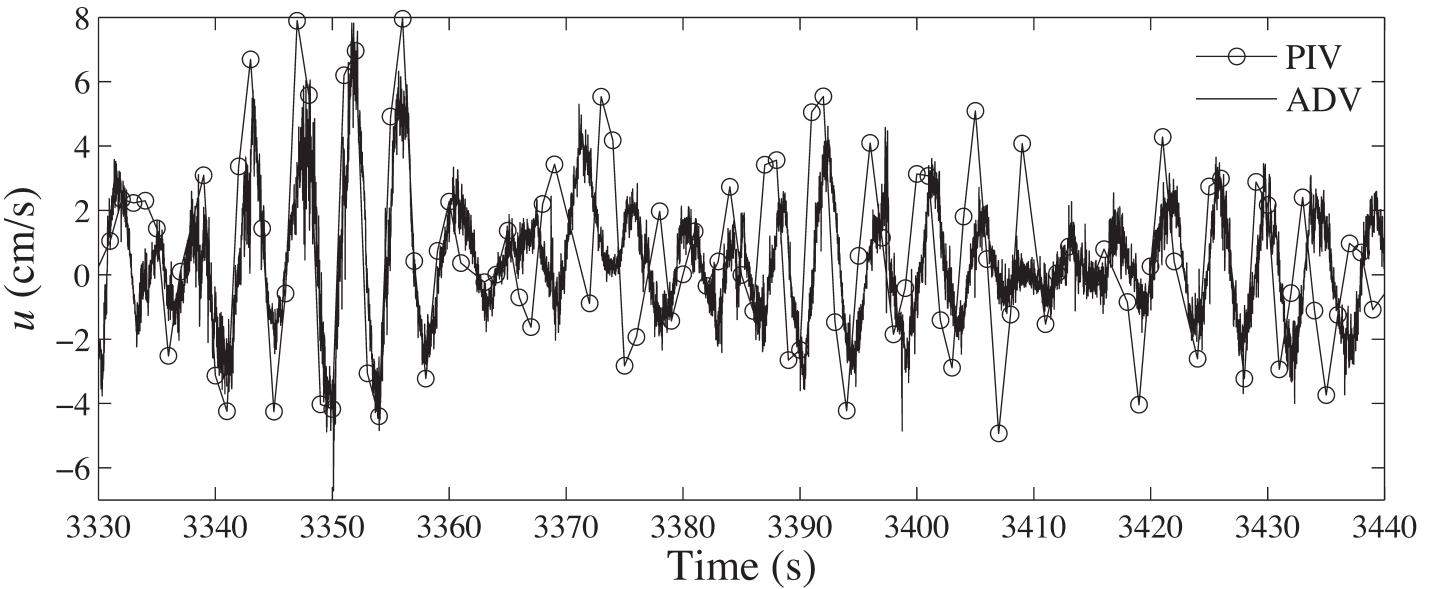


Fig. 7. Comparison between PIV and ADV measurements on 19 Sep 2007. Time represents the number of seconds since 14:00. The ADV was sampled at 64 Hz, and the PIV was sampled at 1 Hz. The sample volume of the PIV probe was at $z = 12$ cm and about 1 m away from the PIV laser plane in the spanwise direction.

One of the objectives of our current research is to characterize the particle consumption rate of dreissenid mussels through filter feeding. Individual particles are identified on PIV images through an in-house MATLAB program using the image-processing toolbox. Procedures of the program are summarized as: (i) A background image is generated based on the local median value of image intensities;

(ii) The background image is subtracted from the original image to form a corrected image; (iii) A binary image is then generated from the corrected image: the pixel value of the binary image is set to “1” if the image intensity is higher than a threshold value, which is set to be the local median grayscale value on a 10×10 pixel stencil, or “0” otherwise; (iv) A topographic analysis is applied to the binary

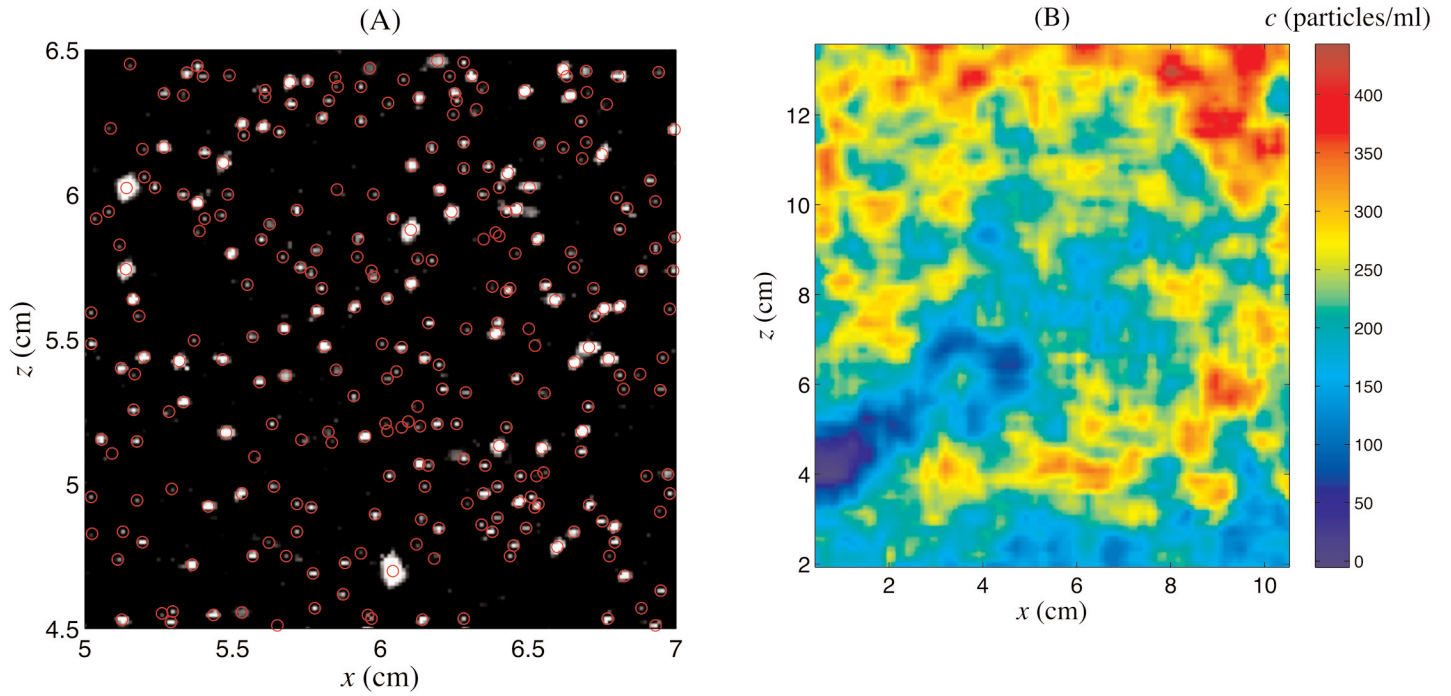


Fig. 8. (A) An example of particle locating result, with each circle marking out the location of an identified particle. (B) An instantaneous particle concentration field resolved on the same grid map of that of PIV interrogations (from data set A31). The concentration on each grid point is evaluated by counting the number of identified particles in a sub-window of 41×41 pixels (5×5 mm) centered on the grid point. The concentration is converted to “particles per milliliter” assuming the thickness of the laser sheet is 3 mm

image to identify the position and area of particles. The pixels with values of “1”s that are next to each other through their four neighbor positions (top, bottom, left and right) are considered as “connected” and grouped together by assigning the same id numbers. The position of one identified particle is defined by the geometric centroid of the grouped pixels, the area of the particle image is determined from the number of these pixels, and the size of particle is taken as the diameter of a circle that has the same area of the grouped pixels; (v) Particle concentration in terms of number of identified particles in a small sub-window is then calculated. It can be converted to number concentration per volume assuming the thickness of the laser light sheet is 3 mm (from the manufacturer’s specification). Fig. 8 shows the result of the particle identification procedures and the calculated instantaneous particle concentration distribution from a sample PIV image.

Assessment

In order to assess the performance of UWPIV, we select the S20 data set for analysis in which the flow was characterized by a relatively strong current (with $U_{z=7\text{ cm}} = 8 \text{ cm s}^{-1}$) superimposed with appreciable surface wave motions (estimated nearbed wave-induced velocity is about 10 cm s^{-1}). The device was deployed by divers at a relatively flat region where the

mussel-covered lakebed was visible in the acquired images. Here we present the calculated statistics of flow in a period of 5 minutes (300 image pairs), during which the mean current velocity near the bed did not show any noticeable trend of change (see Fig. 6, for $t = 201$ to 500 second on 20 September). Before the measurement results are discussed in detail, the overall vertical profiles of velocity and particle concentration superimposed on a raw PIV image are presented in Fig. 9. It shows the overall structure of both the momentum and particle concentration boundary layer near the bed and how the coordinate system is defined.

Profiles of mean velocities, dissipation rate and turbulent flux of particles are horizontally averaged over 45 columns of each instantaneous map, then followed by ensemble averaging over 300 realizations. Therefore each point on a profile is a statistical mean of 13,500 realizations, which is sufficient to achieve a good convergence. Among all the ensemble-averaged quantities, the dissipation rate usually has the largest variability, as the turbulence at the dissipative scale is highly intermittent. The ratio of the standard deviation to the mean, i.e., the coefficient of variation can be as high as 4. Thus the highest standard error for the dissipation rate is only $4/\sqrt{13,500} = 3.5\%$. Profiles of Reynolds stresses are obtained using a spatial correlation method. As we show below, their standard errors are much higher.

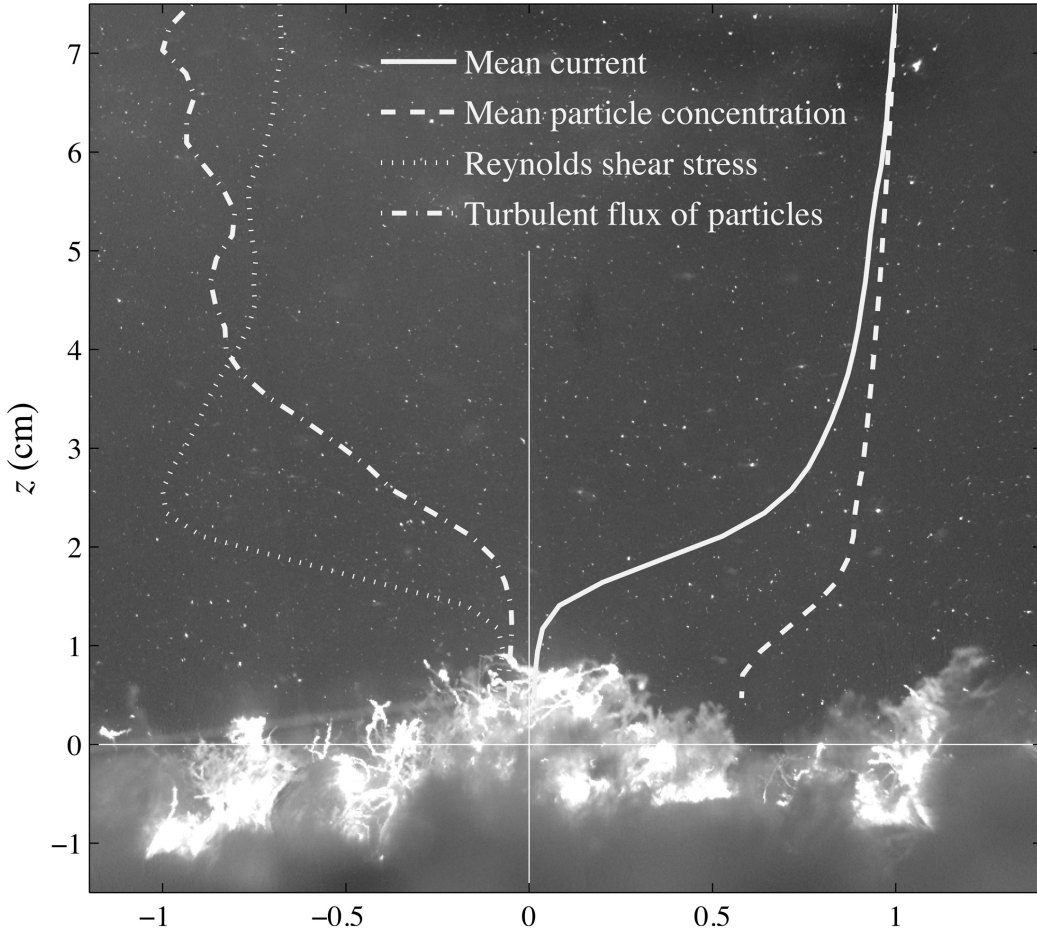


Fig. 9. Coordinate system of the PIV measurement on 20 Sept 2007 and the normalized profiles of 1) mean current velocity, 2) mean particle concentration, 3) turbulent Reynolds stress, and 4) vertical turbulent flux of particle. All profiles are normalized by their maximum magnitude in the range of $0 < z < 7.5$ cm. Maximum values for mean current, mean particle concentration, Reynolds stress, and flux of particle are 8.1 (cm s^{-1}), 21.2 (particles mL^{-1}), 0.263 ($\text{cm}^2 \text{s}^{-2}$), and 0.72 ($\text{particles cm}^{-2} \text{s}^{-1}$), respectively.

Profile of mean current—According to the classical wave-current boundary layer theory (Grant and Madsen, 1979) two log-law layers exist above a wave-affected rough bottom:

$$U = \frac{u_{*c}}{\kappa} \left| \frac{u_{*c}}{u_{*cw}} \right| \ln \frac{30z}{k_b}, \quad \text{if } z < \delta_w \quad (5.1)$$

$$U = \frac{u_{*c}}{\kappa} \ln \frac{30z}{k_{bc}}, \quad \text{if } z > \delta_w \quad (5.2)$$

where $\kappa = 0.41$, the von Karman's constant, u_{*c} is the current-induced shear velocity, u_{*cw} is the wave-current combined shear velocity, k_b is the bed roughness, k_{bc} is the effective roughness with combined effects of bed and wave, and δ_w is the wave-current boundary layer thickness, estimated to be

$$\delta_w = \frac{2\kappa |u_{*cw}|}{\omega} \quad (6)$$

where ω is the angular frequency of the wave. In the present case, δ_w is estimated to be about 1.0 cm given that the wave energy peaked at a period of 4.5 seconds according to spectral

analysis (not shown here), and the estimated maximum shear velocity $u_{*cw} \approx 1.8$ cm s^{-1} . Fig. 10 shows the measured mean current profile plotted in a semi-log fashion. The log-law profile is evident for $z > \delta_w$ (i.e., Eq. (5.2)). Least square curve fitting with the log-law indicates the current induced shear velocity is $u_{*c} = 0.6$ cm s^{-1} and the apparent roughness height, with the combined effects of bottom roughness and wave motions, is $k_{bc} = 1.35$ cm. It is not clear if the log-law within the wave-current boundary layer, Eq. (5.1), is present. The resolution of PIV measurement may not be fine enough to resolve the log-law structure if it ever exists in the wave-current boundary layer, or the flow could be further complicated by *Cladophora*, a filamentous algae that grows above the quagga mussels.

Reynolds stresses—For a turbulent boundary layer flow with surface wave induced motions, the instantaneous velocity can be conceptually decomposed into three parts,

$$u_i(x_i, t) = U_i(x_i) + \tilde{u}_i(x_i, t) + u'_i(x_i, t) \quad (7)$$

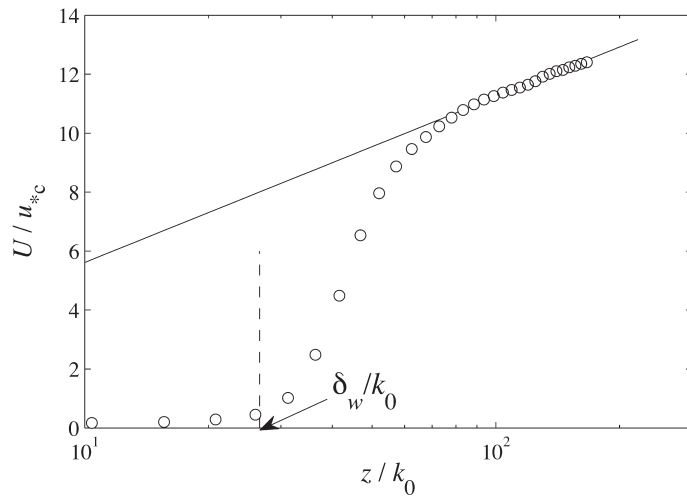


Fig. 10. Vertical profile of the mean current velocity, U , where $u_{*c} = 0.66$ (cm s^{-1}) is the current-induced shear velocity, k_0 is the hydraulic roughness, and $k_0 = k_b/30 = 0.45$ mm. The solid line represents a log-law profile. The dashed line marks the estimated height of the wave-current boundary layer, $\delta_w = 1.0$ cm.

where U_i is the ensemble mean current velocity, \tilde{u}_i is the wave induced oscillating velocity and u'_i is the turbulent fluctuation. In a benthic boundary layer, turbulence is of the most concern for many applications such as the suspension of sediments, dispersal of pollutants, and the flux of solutes into or out of the sediment. The structure of turbulence can be characterized by the Reynolds stress, $\overline{u'_i u'_j}$, (i.e., the covariance of fluctuating velocity components). The oscillating velocity from a wave, however, is irrotational. Hence it does not directly contribute to turbulent mixing although it will interact with turbulence in various ways.

It is not always practical to separate \tilde{u}_i from u'_i as both of them are random in nature. In order to estimate the turbulent Reynolds stresses, means have to be taken to remove the wave contamination from the ensemble-calculated correlations among the three fluctuating or oscillating velocity components. This can be done through the second order structure function $D_{ij}(\bar{r})$, the covariance of the two velocity components u_i and u_j at two locations separated by a vector \bar{r} . While detailed analysis can be found in Nimmo Smith et al. (2002), here the “structure function method” can be summarized as follows: Taking the separating vector \bar{r} as being parallel to the direction of the mean current (x -direction), and assuming the structure function is homogeneous horizontally, D_{ij} is then only a function of height z and separation length r , thus

$$D_{ij}(r, z) = \overline{[u_i(x, z) - u_i(x+r, z)][u_j(x, z) - u_j(x+r, z)]} \quad (8)$$

It can be shown that $D_{ij}(r, z) \approx 2\overline{u'_i u'_j}$ when (i) r is larger than the integral length of the local turbulence (thus $u'_i(x)$ and $u'_i(x+r)$ are statistically uncorrelated) and (ii) r is much smaller than the wavelength of surface waves (hence $\tilde{u}_i(x) \approx \tilde{u}_i(x+r)$).

In the presented study, PIV allows us to estimate the three in-plane Reynolds stresses,

$$\overline{u'^2} \approx \frac{1}{2} D_{11}(r), \quad \overline{w'^2} \approx \frac{1}{2} D_{33}(r) \quad \text{and} \quad \overline{u'w'} \approx \frac{1}{2} D_{13}(r)$$

following the “structure function method.” Fig. 11 shows the structure functions D_{11} , D_{33} and D_{13} measured at $z = 1, 2, 3, 4, 5, 6$ and 7 cm above the bed. For all the cases, the structure function appears to asymptotically reach a constant value as r becomes larger. Since structure functions are calculated based on spatial cross-correlation, the number of point pairs that are available for averaging decreases with the separation distance r : from 13,500 to 2,700 for r changes from 0 to 8 cm. Correspondingly the standard error of averaging can increase significantly for $r > 5$ cm. It ranges from 2~4% of the ensemble mean for D_{11} and D_{33} , and 5~7% for D_{13} . As shown in Fig. 11, there are more fluctuations for D_{13} , which can be attributed to its higher variability. Our previous experience with lab PIV measurements in turbulent boundary layers also suggests that more samples are usually needed for $u'w'$ to converge than those for u'^2 and w'^2 , since the coefficient of variance of $u'w'$ is about 2~3 times higher than that of u'^2 and w'^2 .

Taking the averaged value of $D_{ij}(r > 5 \text{ cm})$ as the asymptotical constant, the Reynolds stresses can be estimated. The resulting profiles normalized by the square of the current shear velocity, u_{*c} , are shown in Fig. 12. The shape and the maximum magnitude of the Reynolds stresses match well with those of canonical boundary layer turbulence at low to medium Reynolds number. For example, Direct Numerical Simulation (DNS) of a channel flow at $\text{Re} = 13,750$ (Kim et al. 1987) indicates that near wall peak stresses for u'^2 , w'^2 , and $-u'w'$ normalized by the square of shear velocity are 7.5, 1.0 and 0.8, while our measured values are 11.2, 2.1, and 0.7, respectively. However, without removing the wave effect, the directly calculated correlations of fluctuations have peak values of 34, 2.4 and 1.3 for normalized u'^2 , w'^2 , and $-u'w'$, respectively. Therefore, surface waves seem to have insignificant impact on w'^2 .

Dissipation rate of TKE—With PIV measured data, the dissipation rate of TKE can be “directly” calculated from the instantaneous 2D in-plane velocity gradients, following Doron et al. (2001), i.e.,

$$\varepsilon_D = 3\nu \left[\left(\frac{\partial u'}{\partial x} \right)^2 + \left(\frac{\partial w'}{\partial z} \right)^2 + \left(\frac{\partial u'}{\partial z} \right)^2 + \left(\frac{\partial w'}{\partial x} \right)^2 + 2 \frac{\partial u'}{\partial z} \frac{\partial w'}{\partial x} + \frac{2}{3} \frac{\partial u'}{\partial x} \frac{\partial w'}{\partial z} \right] \quad (9)$$

This method is not truly a “direct” method since it assumes that the ensemble mean of the missing out-of-plane cross gradients is statistically equal to their in-plane gradients. Alternatively, we can also assume that turbulence in a boundary layer is locally axisymmetric (George and Hussein, 1991), thus

$$\varepsilon_{AS} = \nu \left[- \left(\frac{\partial u'}{\partial x} \right)^2 + 8 \left(\frac{\partial w'}{\partial z} \right)^2 + 2 \left(\frac{\partial u'}{\partial z} \right)^2 + 2 \left(\frac{\partial w'}{\partial x} \right)^2 \right] \quad (10)$$

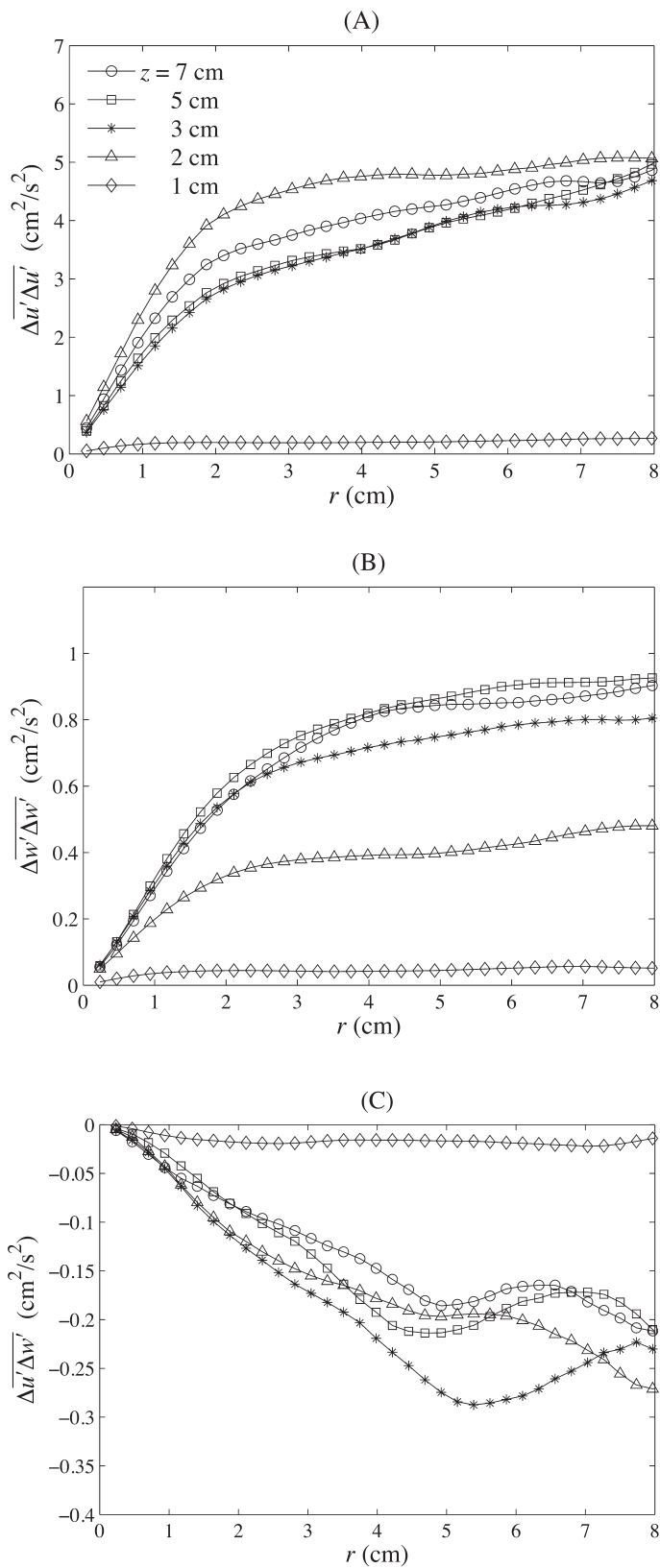


Fig. 11. Structure functions in the streamwise direction calculated on 5 elevations.

Both methods do not rely on the existence of a $-5/3$ slope in the one-dimensional velocity spectra or the assumption that turbulence is locally isotropic. The $-5/3$ slope may not be observed for low Reynolds number flow, and the assumption of local isotropy is usually not valid close to the wall. Therefore “direct” methods are advantageous over spectral methods since fewer assumptions are made. A forward finite differencing method was applied to estimate the instantaneous spatial gradients in Eq. (9) and (10). The ratio of the PIV grid resolution to the average Kolmogorov scale (η) for A31, S19 and S20 are about 4, 2, and 5 respectively (see Table 1). Cowen and Monismith (1997) estimated that 99% of dissipation will be included with finite differencing if the PIV grid size is smaller than 5.5η . Therefore, the resolutions of all three datasets are high enough to resolve turbulence at dissipative scales except near the bottom in S19 and S20 where dissipation rate gets substantially higher.

Fig. 13 presents the measured dissipation rate profile of the S20 dataset using the two “direct” methods. The measured ε_{AS} was systematically lower than ε_D . This is also observed by Doron et al. (2001) in their measurements in a coastal ocean bottom boundary layer. As the law of wall (LOW) suggests that TKE production is locally balanced with dissipation, we also present the measured production rate in Fig. 13, i.e.,

$$P = -\overline{u'w'} \frac{\partial U}{\partial z}.$$

As can be expected, the production is substantially smaller than ε_D and ε_{AS} since it was only the production through the mean current. In other words, the difference from P to ε_D or ε_{AS} can be considered as the production of turbulence due to wave effects. Fig. 13 also shows that the LOW, i.e., $\varepsilon = u_*^3(\kappa z)^{-1}$ is a good estimate for flow above the wave-current boundary layer whose thickness is estimated to be about 1 cm. Within the wave-current boundary layer, the dissipation rate is much higher than that predicted by the LOW, due to wave-current interactions.

The profiles of dissipation rate for all the 3 datasets are also presented in Fig. 14 for comparison. For the S19 dataset, the dissipation within the wave boundary layer is comparable to that of S20 even though the current is almost zero. This result attests to the importance of wave effects on mixing processes in the bottom boundary layer of nearshore waters. The overall magnitude of measured dissipation rates at higher elevations (e.g., $z > 5 \text{ cm}$) is about $10^{-6}\text{--}10^{-5} \text{ m}^2\text{s}^{-3}$. They are comparable with those previously published values measured in coastal oceans (Simpson et al. 1996; Sanford and Lien 1999; Doron et al. 2001) and lakes (Wüest et al. 2000). None of these previous studies was able to measure dissipation rate right above the bed, while in this study the peak value of measured near-bed dissipation rate ($z < 5 \text{ cm}$) is about 1~2 orders of magnitude higher than that is found slightly above the bed.

Through the measured data, it is difficult to reach a conclusion as to whether filtering activities of mussels may have any important effects on turbulence structures. In order to estimate the effects of mussel activities, we also measured the vertical profile of dissipation rate over a cultivated quagga

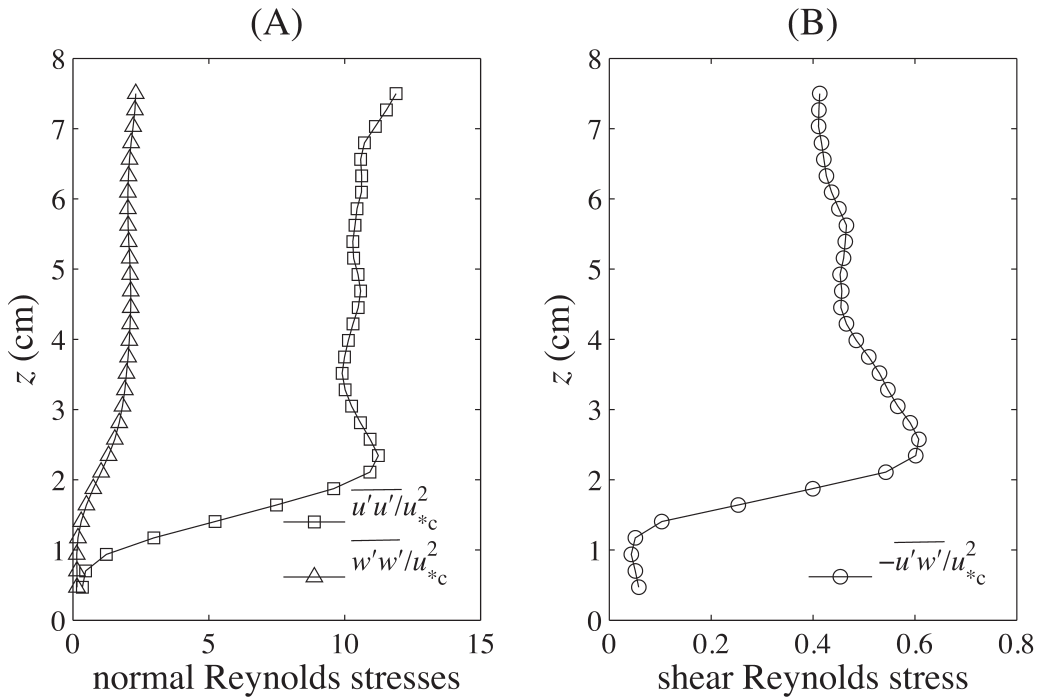


Fig. 12. Vertical profiles of Reynolds stresses normalized by the square of current shear velocity u_c .

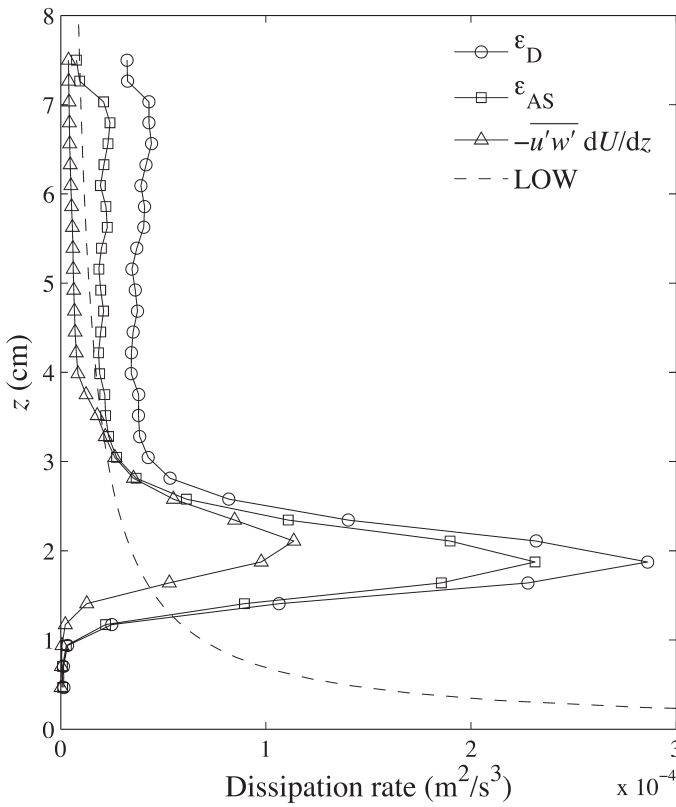


Fig. 13. Estimates of dissipation rate of turbulent kinetic energy with different methods: “direct” method (ϵ_D); local axisymmetric assumption (ϵ_{AS}); local balance with production rate; law of wall.

mussel bed in a laboratory aquarium. In the lab experiment, no external current was imposed, and the water mass was mainly stirred by the bivalves’ siphon currents which can be triggered by adding algal particles in the aquarium. As shown in Fig. 14, measured dissipation rate is on the order of $10^{-6} \text{ m}^2 \text{ s}^{-3}$ near the bed within a layer of about 4~5 cm thick. It then decreases rapidly with height. This indicates that the hydrodynamic effect of mussels’ filtration only extend to a height of 4~5 cm. It also shows that the measured dissipation rate is about two orders of magnitude smaller than that in a nearshore bottom boundary layer, and therefore may not substantially affect the structure of boundary layer turbulence under flow conditions comparable to what we have observed on the three deployment dates.

Turbulent flux of particle concentration—Through our preliminary deployment in Lake Michigan, we have also demonstrated that the UWPIV can quantify the turbulent flux of particles (mainly phytoplankton and sediment particles), thus the uptake rate of plankton by mussels could be estimated. From the S20 dataset described above we have found that during a period of 250 seconds the particle concentration increased with time at all observed heights above the lakebed (see Fig. 15(A), 15(B)). The overall trend of increase is quite linear. This increase was accompanied by a net downward turbulent flux of particles, i.e., $w'c' < 0$, and the existence of a concentration boundary layer. The most noticeable feature of the mean concentration profile is a sharp gradient region above the mussel bed (see Fig. 9). The thickness of this region is about 1.5~2 cm. Considering a water column with a unit cross-sectional

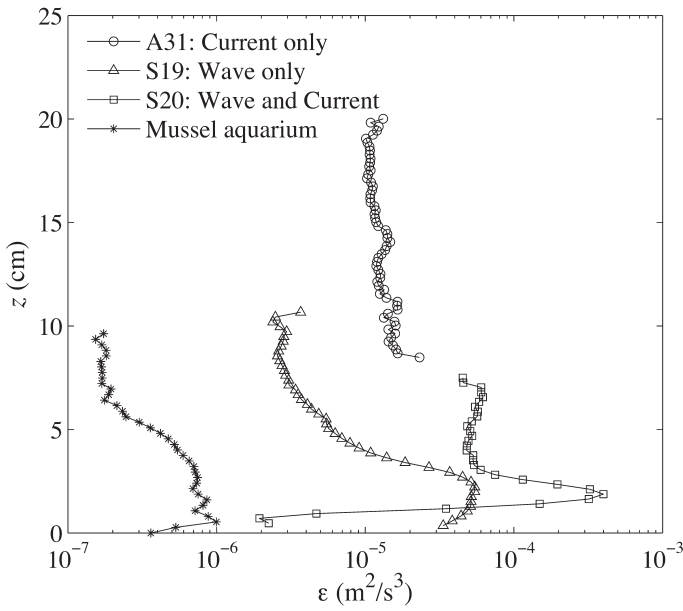


Fig. 14. The vertical profiles of dissipation rate of the three datasets: A31 (averaged over 62 s), S19 (averaged over 785 s), and S20 (averaged over 300 s). The dissipation rate (averaged over 300 s) of the turbulence generated by mussels' siphon currents in a small lab aquarium is also presented.

area above the mussel bed with height = z , the mass balance of particles in the column can be approximated as

$$\frac{d \int_0^z C(z', t) dz'}{dt} = -\bar{w}' c' + G \quad (11)$$

where $C(z, t)$ is the linear regression of the mean concentration (the dashed line in Fig. 15(B)), and $c'(z, t) = c(z, t) - C(z, t)$, the deviation of the instantaneous concentration from the linearly increasing mean; and G is the sink term representing the mussel grazing rate of particles. Here we have ignored the net horizontal fluxes due to the mean current and turbulence, as the measured mean particle concentration is horizontally uniform. The net turbulent flux in the horizontal direction is also negligible. Also the measured mean vertical velocity is of the order of -0.01 mm s^{-1} , which can be considered as the average settling speed of particles. The depth averaged vertical flux due to particle settling is about $0.1 \text{ particles cm}^{-2} \text{ s}^{-1}$, about 3% of the vertical turbulent flux. Hence the settling effect is ignored as well. Moreover, we are not able to evaluate the resuspension of particles from the bed, it is just simply excluded from the approximated model Eq. (11).

The vertical profiles of mean increase rate of total particles and the turbulent flux are shown in Fig. 15(C), and the difference of them is assumed to be the grazing rate, G , according to Eq. (11). This grazing rate is shown to be approaching a constant value for $z > 4 \text{ cm}$, while it gradually decreases as approaching to the bed. The reduced G near the bed could be due to particle resuspension that we have ignored. It is also possible that particles are removed by out-of-plane siphon

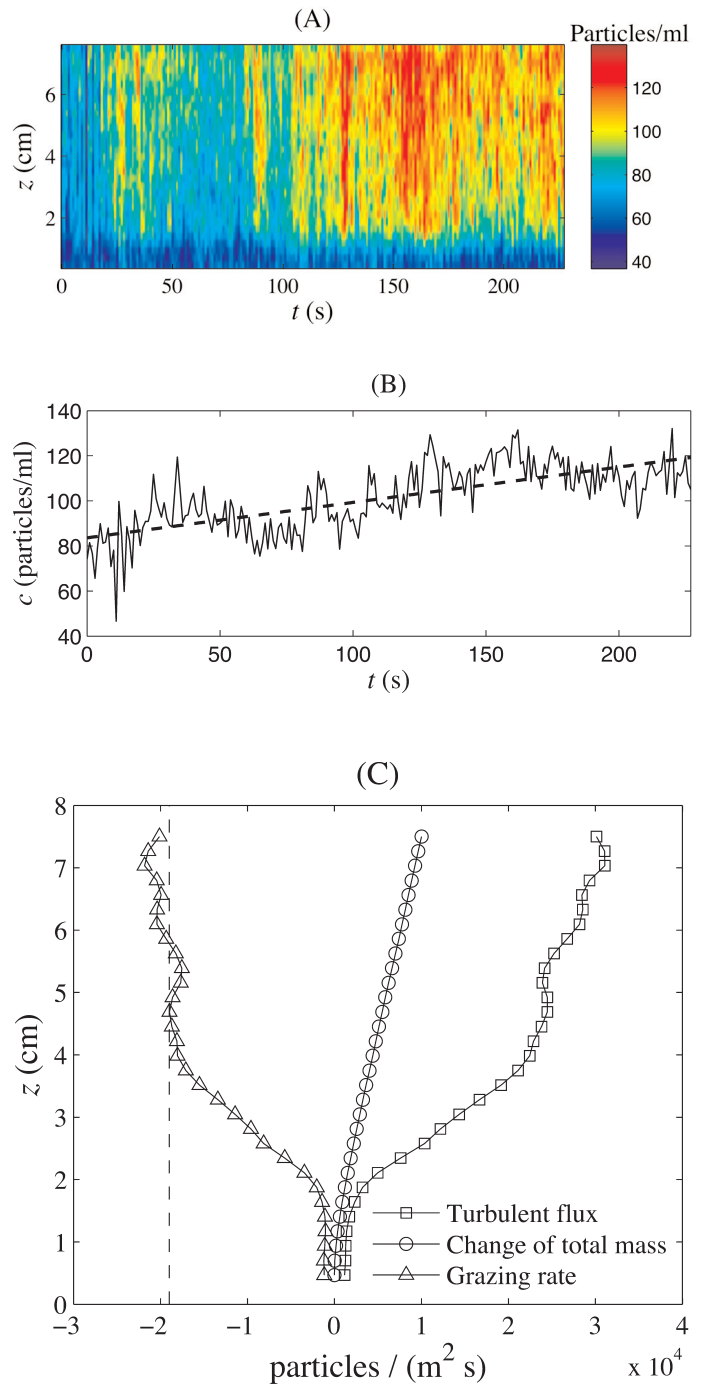


Fig. 15. (A) A time series of the vertical profile of particle concentration (averaged over the width of the image) during a period of 250 s. (B) Change of concentration over time at $z = 7 \text{ cm}$. The dashed line represents a linear regression with time, which is considered as the mean concentration, $C(z, t)$. (C) Vertical profiles of the turbulent flux $-\bar{w}' c'$, rate of change total particles $d\left(\int_0^z C dz'\right)/dt$, and the estimated mussel grazing rate G . The estimated grazing rate approaches to a constant value approximately for $z > 4 \text{ cm}$, shown as the dashed line, which is about $1.9 \times 10^4 \text{ particles m}^{-2} \text{ s}^{-1}$.

currents generated by mussels sitting at a small distance away from the image plane. This effect may result in a distributed sink term over a height of about 4 cm. Nevertheless, if the balance of particles is analyzed over a water column higher than 4 cm, the overall grazing rate measured during this 250-second period is about 1.9×10^4 particles $\text{m}^{-2} \text{s}^{-1}$.

Turbulent viscosity and turbulent diffusivity—For the S20 dataset where a strong mean current existed, the smoothness of the measured velocity profile allows us to calculate its vertical gradient using central finite differencing method. Thus the turbulent viscosity can be directly estimated as:

$$\nu_T = \frac{-\bar{u}'\bar{w}'}{dU/dy}.$$

Similarly the turbulent diffusivity can be directly calculated as

$$D_T = \frac{-\bar{w}'\bar{c}'}{dC/dy},$$

and it compares well with the turbulent viscosity (Fig. 16). Both of them increased approximately linearly with elevation z , although they are all smaller than that of the LOW, i.e., $\nu_T, D_T = \kappa u_* z$ (the straight line in Fig. 16), based on the estimated shear velocity from the log-law profile of the mean current.

Discussion

Small-scale turbulence in environmental fluid flows, i.e., in rivers, lakes, oceans and wetlands, is an important factor that controls and limits many environmental transport processes, especially those near a physical interface such as the bottom boundary, air-water interface, and water-vegetation interface. Traditional turbulent velocity measurement devices in field studies are usually limited to one point or along a line in space, and they lack the resolution to characterize the turbulence at dissipative scales. The UWPIV presented here can solve these problems by producing 2D high-resolution velocity measurements. Using a scanning mirror to deliver low-power CW laser light into the flow field is the key to ensure adequate illumination of small particles ($\sim 10 \mu\text{m}$), which are abundant in natural waters, and to keep the particle exposure time short at the same time. Since the exposure time for the CCD sensor needs to be relatively long ($>$ laser scanning time), it is also critical to use a narrow band-pass optical filter to block the strong ambient light if the experiment has to be conducted during daytime and in shallow water. All components of the UWPIV system can be obtained off-the-shelf, thus it can be easily adopted by any interested researchers.

Three preliminary experiments were conducted in a turbulent wave-current boundary layer at a nearshore site in Lake Michigan over a quagga mussel covered bed. The profiles of the in-plane components of the Reynolds stresses can be measured using the structure function method, such that wave induced random oscillations can be excluded from the measured stresses. This is one advantage of PIV over point or profile measurement devices, as 2D spatial distribution of velocities are available. The structure function method requires that the images size is greater than the integral length of the

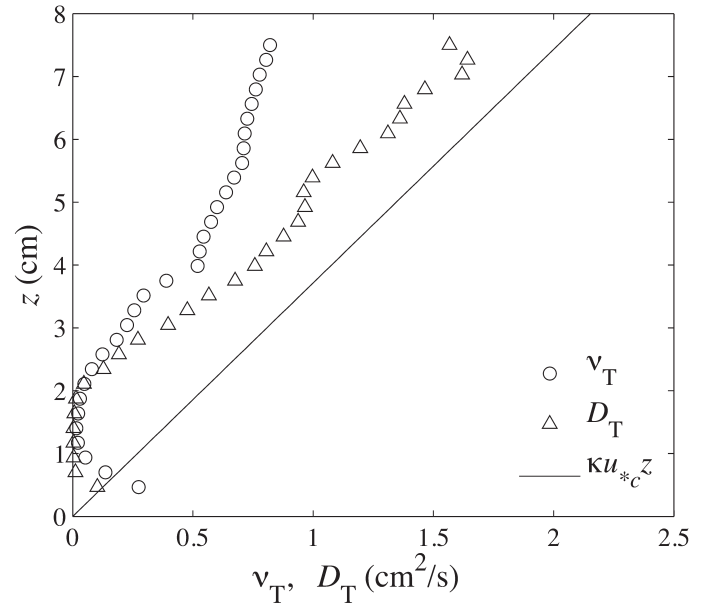


Fig. 16. Vertical profiles of turbulent viscosity and turbulent diffusivity of particle concentration.

turbulence. For measurements in bottom boundary layers, this requirement can be satisfied since the integral length is limited by the height above the bottom. For measurements in an elevated location where the integral length becomes much larger, either the in-plane structure function needs to be extrapolated, or a two-camera configuration is required (Nimmo Smith et al. 2002). Alternatively, Luznik et al. (2008) proposed to estimate Reynolds stresses using PIV measurement according to the following decomposition

$$u'_i = u_i - \left(\langle u_i \rangle_I - \overline{\langle u_i \rangle}_I \right) \quad (12)$$

where u'_i is the instantaneous turbulent fluctuation, u_i is the measured instantaneous velocity, $\langle u_i \rangle_I$ is the spatially averaged velocity over one image, and $\overline{\langle u_i \rangle}_I$ is the temporally low-pass filtered, image-averaged velocity (with frequencies smaller than those of surface waves), which is considered as large scale turbulent motion. Again, this method takes advantage of 2D PIV measurement, and the detailed analysis should appear in publications soon (personal communication with Luznik). TKE dissipation rate is one of the most important parameters to quantify the characteristics of small-scale turbulence. The resolution of the UWPIV system allows the dissipation rate to be estimated using a “direct” differentiation method. This method does not rely on the existence of a $-5/3$ slope in the turbulent velocity spectrum and the assumption of local isotropy, thus it is applicable to flows with low Re number or flows near an interface, where turbulence can be very anisotropic. To the authors’ knowledge, the UWPIV system presented here is the first that is able to resolve the near-wall dissipation rate profile in coastal ocean or lake bottom boundary layers. Particle concentration measurement is feasible and a constant turbulent

flux layer is observed as an expected result of mussel filtration. However, the measured concentration is limited to particles that can be detected by the current optical configurations. Scattered light from smaller particles might be too weak to be imaged by the CCD chip or to be identified by the particle finding program. In future studies, more rigorous calibrations will be performed to validate this method.

Comments and recommendations

The UWPIV system presented in the paper costs about \$13K. Among all the components, the 12-bit CCD camera is the most expensive part at \$7.5K. The cost can still be significantly reduced if a 10-bit pixel resolution camera is adopted. We have tested this option using a Unibrain IEEE1394 camera (Fire-i 601), which costs only \$2.3K. Although the dynamic range of the intensity of a particle's image is reduced by 75%, we found this does not noticeably affect the quality and accuracy of PIV interrogations.

The FOV in the preliminary tests is about 14 cm on both edges, which is adequate for studying the boundary layer structures over the quagga mussel beds, as the measured particle concentration boundary layer was about 8 cm. Larger FOV can be achieved through widening the light sheet and the view of angle, at the expense of shorter particle exposure time, if the scanning time is kept the same. Currently, compact DPSS lasers with higher power (500mW~2W) are becoming available on the market, thus we expect the FOV of the system could be increased up to about 1 m without sacrificing the quality of particles' images. Also, the distance of the object plane from the camera lens (48 cm for the current system) might need to be increased in order to obtain a larger FOV. In such a case, the turbidity of water becomes an issue, as a greater portion of reflected light will be absorbed before reaching the camera. This might not be a problem for most measurements in lake and ocean environments, but will be critical for applications in rivers and in the surf zone of lakes and oceans where turbulence and concentrations of suspended sediment are much higher.

The UWPIV system presented here can measure a flow speed up to about 20 cm s⁻¹ with moderate levels of turbulence. Both in-plane (due to high rotation and straining rate) and out-of-plane loss of correlation will arise for flow with higher speeds and turbulence. This problem can be solved by decreasing the scanning time (thus a smaller ΔT) at the expense of weaker illumination. At a certain limit (e.g., tidal currents or river flow with speed on the order of 1 m s⁻¹ or higher), the UWPIV may fail to work. We propose to use a two-laser two-camera configuration to overcome this difficulty. Two laser beams with different colors (e.g., 532 nm and 473 nm) can be guided to the center of a galvanometer with an angle difference, θ . Therefore, the two beams will pass through a given spatial location with a time lag $\Delta T = \theta/\Omega$, where Ω is the angular speed of the rotating mirror. This time lag can be adjusted by regulating the angle difference θ

and it is not limited by the scanning time T_s . A particle on the object plane will be illuminated twice during one scan, separated by an approximate time difference of ΔT , assuming that the displacement of the particle during ΔT is small compared with the separation distance of the two beams. Otherwise, the exact time lag between the two exposures, which depends on the speed of the moving particle, can still be estimated as the locations of the two exposures are known. Two cameras with corresponding optical filters will be applied to take images of the particles, i.e., the system can be designed in a way that the scattered light of one color will be imaged on one camera while being invisible to the other camera, and vice-versa.

The UWPIV can also be designed as a free-falling profiler, similar to the system developed by Steinbuck et al. (2004). In such a configuration, the measured velocity field includes the descending speed of the device. It might not always be possible to separate the motion of the device from the distributions of the absolute fluid velocity. However, the small-scale structures, such as the distributions of vorticity, rate of strain and dissipation rate, which are based on the spatial gradient of velocities, will not be severely influenced by the rigid-body translation and rotation. For the same reason, it can be designed as a floating device that measures the wind-generated turbulence near the air-water interface. Profiles can be obtained just below the interface for dissipation rate, enstrophy, and surface divergence. Such measurements would facilitate the study of air-water interactions, as the dissipation rate below the interface is considered an important parameter that determines the transfer speed of low-solubility gases such as CO₂, O₂, and other climatically important gases (Zappa et al. 2007).

The UWPIV could be improved in many ways for long-term observation purposes. For example, if the system is designated to measure the vertical profiles of a coastal bottom boundary layer over several hours or longer times, it could be equipped with guiding vanes to adjust its orientation to the shifting mean current direction to avoid the out-of-plane loss of particles. Finally, long-range monitoring devices, such as ADCPs and thermistor strings, should always be deployed in company with UWPIV to provide information about the larger scale dynamics, as a background to the measured small-scale turbulence.

References

- Adrian, R. J. 1991. Particle imaging techniques for experimental fluid mechanics. *Annu. Rev. Fluid Mech.* 20:421-485.
- Bertuccioli, L., G. I. Roth, J. Katz, and T. R. Osborn. 1999. A submersible particle image velocimetry system for turbulence measurements in the bottom boundary layer. *J. Atmos. Oceanic Technol.* 16:1635-1646.
- Clarke, J., A. Cotel, and H. Tritico. 2007. Development, testing and demonstration of a portable submersible miniature particle imaging velocimetry device. *Meas. Sci. Technol.* 18:2555-2562.

- Cowen, E. A., K. -A. Chang, and Q. Liao. 2001. A single-camera coupled PTV-LIF technique. *Exp. Fluids* 31(1):63-73.
- and S. G. Monismith. 1997. A hybrid digital particle tracking velocimetry technique. *Exp. Fluids* 22:199-211.
- Doron, P., L. Bertucciol, J. Katz, and T. R. Osborn. 2001. Turbulence characteristics and dissipation estimates in the coastal ocean bottom boundary layer from PIV data. *J. Phys. Oceanogr.* 31:2108-2134.
- George, W. K., and H. J. Hussein. (1991) Locally axisymmetric turbulence. *J. Fluid Mech.* 233:1-23.
- Grant, H. L., and O. S. Madsen. 1979. Combined wave and current interaction with a rough bottom. *J. Geophys. Res.* 84:1797-1808.
- Katija, K., and J. O. Dabiri. 2007. In situ field measurements of aquatic animal-fluid interactions using a Self-Contained Underwater Velocimetry Apparatus (SCUVA). *Limnol. Oceanogr. Methods* 6:162-171.
- Kim, J., P. Moin, and R. Moser. 1987. Turbulence statistics in fully developed channel flow at low Reynolds number. *J. Fluid Mech.* 177:133-166.
- Luznik, L., E. E. Hackett, J. Katz, and T. R. Osborn. 2008. Direct estimation of the Reynolds stresses from PIV data. 2008 Ocean Science Meeting, Mar. 2~7, Orlando, FL.
- , R. Gurka, W. A. M. Nimmo Smith, W. Zhu, J. Katz, and T. R. Osborn. 2007. Distribution of energy spectra, Reynolds stresses, turbulence production, and dissipation in a tidally driven bottom boundary layer. *J. Phys. Oceanogr.* 37(6):1527-1550.
- Nimmo Smith, W. A. M., P. Atsavapranee, J. Katz, and T. R. Osborn. 2002. PIV measurements in the bottom boundary layer of the coastal ocean. *Exp Fluids* 33:962-971.
- , J. Katz, and T. R. Osborn. 2005. On the structure of turbulence in the bottom boundary layer of the coastal ocean. *J. Phys. Oceanogr.* 35:72-93.
- Sanford, T. B., and R. C. Lien. 1999. Turbulent properties in a homogeneous tidal bottom boundary layer. *J. Geophys. Res.* 104(C1):1245-1257.
- Simpson, J. H., W. R. Crawford, T. P. Rippeth, A. R. Campbell, and V. S. Cheok. 1996. The vertical structure of turbulent dissipation in shelf seas. *J. Phys. Oceanogr.* 26:1579-1590.
- Steinbuck, J. V., C. D. Troy, P. J. Franks, E. Karakoylu, J. S. Jaffe, S. G. Monismith, and A. R. Horner. 2004. Small-scale turbulence measurements with a free-falling DPIV profiler. American Geophysical Union Fall meeting 2004, abstract # OS53B-05, Dec. 13-17, San Francisco, CA.
- Willert, C. E., and M. Gharib. 1991. Digital particle imaging velocimetry. *Exp. Fluids* 10:181-193.
- Zappa, C. J., and others. 2007. Environmental turbulent mixing controls on air-water gas exchange in marine and aquatic systems. *Geophys. Res. Lett.* 34:L10601.1-L10601.6.
- Wüest, A., G. Piepke, and D. C. Van Senden. 2000. Turbulent kinetic energy balance as a tool for estimating vertical diffusivity in wind forced stratified waters. *Limnol. Oceanogr.* 45:1388-1400.

*Submitted 23 April 2008**Revised 24 November 2008**Accepted 23 January 2009*